Pore crystallization and expansion of cement pastes in sulfate solutions with and without chlorides

Bo Ran, Othman Omikrine Metalssi, Teddy Fen-Chong, Patrick Dangla, Kefei Li

Pore crystallization and expansion of cement pastes in sulfate solutions with and without chlorides

Bo RAN[a,b], Teddy FEN-CHONG[b], Othman OMIKRINE-METALSSI[b], Patrick DANGLA[c] and Kefei LI[a,*]

[a]Civil Engineering Department, Tsinghua University, Beijing, 100084, China
[b]Cerema, UMR MCD, Université Gustave Eiffel, Marne-la-Vallée, F-77454, France
[c]Navier, Ecole des Ponts, Université Gustave Eiffel, CNRS, Marne-la-Vallée, F-77447, France

ARTICLE INFO

Keywords:
cement paste
sulfate attack
chloride
ettringite
pore crystallization

ABSTRACT

The pore crystallization of ettringite (AFt) and the material expansion are investigated for cement paste subject to external sulfate attack with and without chlorides. Specimens of 2mm thickness were exposed to solutions of 10g/L Na_2SO_4, 10g/L Na_2SO_4 + 10g/L NaCl and 10g/L Na_2SO_4 + 19g/L NaCl. The evolutions of AFt formation, pore structure, transport property and specimen expansion were characterized through ^{27}Al NMR, MIP, DVS and micrometer measurements. The analysis of results shows that: (1) chlorides decrease the AFt formation rate and the expansion capacity through depressing the supersaturation of AFt crystals; (2) AFt crystallization alters the pore structure in the whole pore size range, especially through the blockage of "ink-bottle" pores in micropore range; (3) AFt crystals change the vapour diffusivity by pore-filling and microcracking, and the linear stage of expansion is well captured by poromechanics with pore crystallization pressure incorporated.

1. Introduction

External sulfate attack (ESA) and chloride ingress are two important concerns of durability for the reinforced concretes exposed to aqueous environments, such as seawater and groundwater[1, 2]. So far, the respective mechanisms of ESA and chloride ingress have been investigated in depth and well identified: the external sulfates react directly with aluminate hydrates in hardened concrete and generates expansive products, ettringite and/or gypsum, resulting in material damage of cracking and spalling[3, 4], while the chloride ingress depassivates the steel reinforcement in concrete and initiates the corrosion with pitting patterns[5]. In natural environments, sulfate and chloride ions usually coexist, and the understanding of their combined action is important to the correct estimate of the service life of structural concretes exposed to such environments.

As sulfate and chloride ions are both present, their interaction is reciprocal, including the impact of sulfates on chloride ingress and the influence of chlorides on sulfate attack. For the former, literature results [6, 7] showed that the chlorides penetrate deeper into concretes under the sulfate-chloride solution than the chloride solution alone. The promoted chloride ingress is attributed to the release of the bound chlorides in solid matrix by sulfates to the pore solution [8, 9]. For the latter, two fundamental aspects are relevant: the formation of ettringite and the physical/mechanical effect of the formed AFt in pores. The majority of literature results confirm the inhibiting effect of chlorides on the sulfate attack [2, 10, 11, 12]. The inhibiting effect of chlorides on the AFt formation has been addressed through two main mechanisms[7, 9, 12, 13]: the increased solubilities of ettringite and gypsum in the chloride-containing solutions, and the transformation of aluminate hydrates into Friedel's salts. The solubilities of ettringite and gypsum were reported to increase by 3.5 times [14] and 3 times [15] respectively when exposed to NaCl solutions compared to water. Actually, this is due to the reduction of ionic activity coefficients, of such weakly soluble solids as ettringite and gypsum, with the increase of total aqueous ionic strength[16]: the Ca^{2+} activity coefficient in gypsum can be reduced from 0.41 in water[17] to 0.17 in 3.08M NaCl solution[18], and a higher Ca^{2+} concentration is needed to maintain the dissolution equilibrium. Following this line, the ionic strength of pore solution in hardend cement pastes is taken as 0.25M[19], and adding groundwater and seawater, equivalent to 0.03M and 0.54M NaCl[20]

*Corresponding author
likefei@mail.tsinghua.edu.cn (K. LI)
ORCID(s): 0000-0003-1635-6362 (K. LI)

into pore solution, will lower the activity of Ca^{2+} and SO_4^{2-} by 1.8% and 30% [19], not increasing substantially the solubility of ettringite or gypsum. Thus, the intervention of chlorides in AFt formation is more plausible: the formation of Friedel's salts in mixed sulfate and chloride solutions reduces the ettringite formation due to the competition between chlorides and sulfates for aluminate phases [1, 2, 21]. However, Balonis et al.[22] reported, through thermodynamic simulations, that the formation of Friedel's salts released sulfates from monosulfoaluminate (AFm) and more ettingite could be generated from the released sulfates. For the physical and mechanical effect of AFt formation, some studies showed clear mitigating effect of chlorides on the strength loss of mortars [10, 12, 13, 23] while others [7] measured similar material expansions for cement mortars exposed to mixed solution and pure sulfate solution. So far, the direct experimental evidence for the role of chlorides on ettringite formation is still in dearth, and the physical and mechanical effect of ettringite crystallization in pores has not yet been treated as an independent subject.

Accordingly, more deepened investigations are needed to clarify the mechanism of the mitigating effect of chlorides on ESA for both the ettringite formation in pores and its effects on physical and mechanical properties of materials. Only through this understanding, the durability of structural concretes exposed to such environments can be correctly designed and predicted. Motivated by this need, this paper attempts to deepen the study of the mitigating effect of chlorides on ESA. To this purpose, the ^{27}Al Nuclear Magnetic Resonance (NMR) and Mercury Intrusion Porosimetry (MIP) are applied to quantify the aluminum phases and characterize the pore structure in cement pastes under pure sulfate attack and combined action of sulfates and chlorides. Besides, the vapour diffusivity and specimen expansion are measured by Dynamic Vapour Sorption (DVS) and micrometer respectively to examine the evolution of transport property and material damage. Two special measures are undertaken in this study: the solutions are regulated at pH=13 to avoid the leaching effect on ESA[24, 25] and thin specimens of 2mm thickness are made to avoid non-uniform distribution of ions and crystallization across the thickness. In the following, the experimental program is presented in Section 2; the experimental results are given in Section 3; the pore-level crystallization is discussed in Section 4; and the concluding remarks are provided in Section 5.

2. Experimental program

2.1. Specimens and exposure solutions

Prisms of 40mm×40mm×160mm were prepared from cement paste with a water to cement ratio (w/c) of 0.55. The cement used is CEM I Type (CEMI 52.5 N CE CP2) with the chemical composition given in Table 1. The mineral contents are evaluated, through Bogue's method[26], as C_3S(65.2%), C_2S(8.8%), C_3A(7.9%) and C_4AF(8.9%). To avoid the leaching during curing process, all the prisms were stored in saturated portlandite (CH) solution with a water to solid ratio (volume) around 26. From the prisms after 60d curing, rectangular slices of 2mm×20mm×120mm and square slices of 2mm×40mm×40mm were sawed out using a high-precision cutting machine. Each rectangular slice specimen was equipped with a pair of stainless-steel pins fixed on the two ends for expansion measurement, cf. Fig.3 in [27], and the square slice specimens were reserved for the characterization tests of NMR, MIP and DVS. These slice specimens were then immersed into three different test solutions. Table 2 presents the composition of these

Table 1
Chemical composition of CEM I cement

Components %										
CaO	SiO_2	Al_2O_3	Fe_2O_3	CaO(free)	MgO	SO_3	S	K_2O	Na_2O	Ignition Loss
62.81	20.22	4.85	2.92	1.58	0.84	2.88	0	0.77	0.34	2.59

Table 2
Composition of sulfate and mixed solutions

Number	SO_4^{2-} concentration	Cl^- concentration	OH^- concentration
C1	10 g/L	0	1 mol/L
C2	10 g/L	10 g/L	1 mol/L
C3	10 g/L	19 g/L	1 mol/L

solutions: two mixed solutions containing 10g/L and 19g/L of chlorides and 10g/L of SO_4^{2-}, and a single sulfate solution containing 10g/L of SO_4^{2-} as the reference solution. Besides, the pH values of three solutions were maintained at 13.0 by adding 1mol/L NaOH to avoid the leaching of cement paste during sulfate reactions. These solutions were renewed on weekly basis (within the first month) and bi-weekly basis (afterwards) to maintain a constant sulfate concentration[28]. At given exposure ages, the square slice specimens were taken out and subject to freeze drying treatment by a freeze-dryer (Christ's Alpha 1-4 LDplus) before the characterization tests.

2.2. Characterization methods

The characterization of slice specimens includes the ^{27}Al NMR for the content of aluminum phases, the MIP for the pore structure, DVS for vapour diffusivity and micrometer for specimen expansion. The principles and technical details of these tests are given in the following.

The ^{27}Al NMR is a powerful technique for the characterization of aluminum hydrates in hardened cement pastes[30]. The aluminium atoms in aluminum hydrates are covalently bound with oxygen atoms in octahedral and tetrahedral configurations. The octahedral configuration corresponds to AFt, AFm and TAH (third aluminum phase) with a chemical shift around 10ppm, and the Al(V) phase with a chemical shift at $\sim$ 35ppm, representing the substitution by aluminum of interlayer Ca^{2+} in calcium silicate hydrate (CSH). The tetrahedral configuration corresponds to the Al(IV) phase, with a chemical shift around 70ppm, denoting the replacement of SiO_4 by AlO_4 tetrahedra in CSH chains[31]. Moreover, a typical ^{27}Al spectrum of cement paste, cf. Figure 1b, contains spinning sidebands as well, which represents the repetitions of major peak signals for AFm, AFt, TAH phases at the spinning frequency. These sidebands are valid signals and need to be considered in the computation of phase content. To capture the contribution of these sideband signals, an extra spectrum with a broader range of -1000$\sim$1000 ppm was measured, cf. Figure 1a. During the test, each sample was examined by 27Al NMR twice, yielding two spectra with the ranges of 300ppm and 2000ppm, cf. Figure 1a and b. The high-precision spectrum in the 300ppm-range was used to decompose the three major peaks of AFt, AFm and TAH around 10ppm for the calculation of their relative contents while the 2000ppm-range spectrum was adopted to calculate the ratio of the major phases AFt, AFm and TAH, sum of their major peaks and spinning sidebands, to the minor phases of Al(IV) and Al(V). The decomposition of major peaks around 10ppm is performed using the multi-peaks fitting approach following [29], cf. Figure 2. This study used a JNM-ECZ600R Solid NMR Spectrometer with a field intensity of 14.09 T. The freeze-dried square slice specimens were ground into

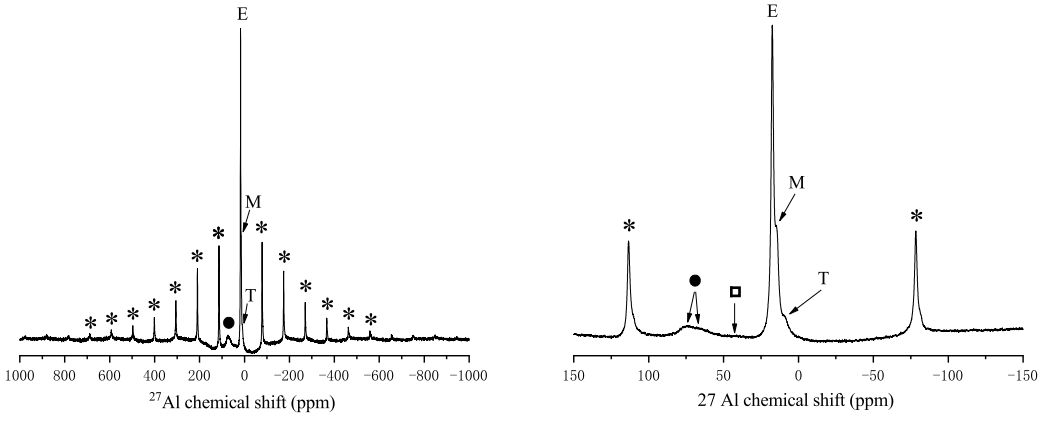

Figure 1: ^{27}Al MAS NMR spectra (magnetic field intensity of 14.09 T, spinning speed of 15 kHz) of cement paste (w/c=0.55) for 84-day exposure to sodium sulfate solution of 10g/L SO_4^{2-}, with ranges of 2000 ppm (a) and 300ppm (b). The symbols E, M and T denote ettringite, AFm and TAH respectively. The asterisk ($*$) stands for spinning sideband from ettringite, AFm and TAH peaks, the filled circle ($\bullet$) for Al(IV) phase, and the square ($\square$) for Al(V) phase.

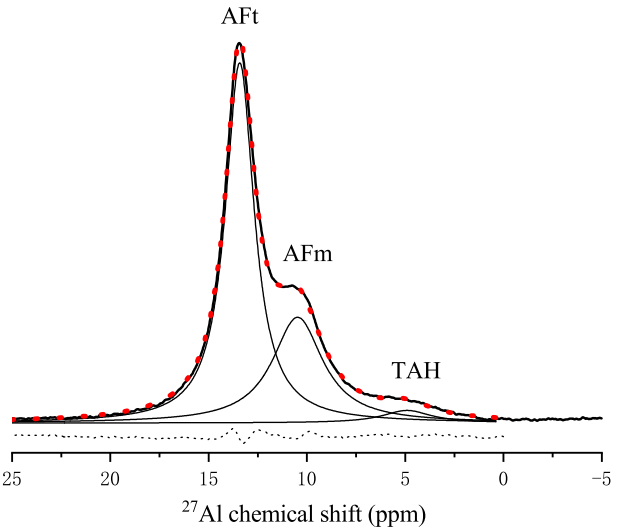

Figure 2: Decomposition of ^{27}Al MAS NMR spectrum of cement paste (w/c=0.55) for 84-day exposure to sodium sulfate solution of 10g/L SO_4^{2-}, using multi-peaks fitting method in [29]. The black solid line represents the experimental spectrum, and the red dotted line is the simulated total spectrum. The solid lines with single peak stand for simulated AFt, AFm and TAH spectra respectively. The lower dotted line represents the difference between simulated and experimental spectra.

powder samples and placed in a tube of 3.2mm diameter with a high spinning frequency of 15kHz.

The DVS is a well-established method for the determination of vapour sorption isotherms through high-resolution mass measurement and stable temperature and humidity control[32]. A diffusion (Payne) cell is set up within the DVS device to measure the water vapor diffusivity, cf. Figure 3a. The DVS device used is an Adventure DVS instrument, weighing the mass of vapor flow to the precision of 0.001mg and controlling the relative humidity (RH) by mixing nitrogen and water vapor to the precision of 0.05% (25°C). The Payne cell is composed of two parts: the cell lid with two O'rings to hold the pellet specimen allowing a maximum thickness of 2.4mm, and the cell cup containing drying

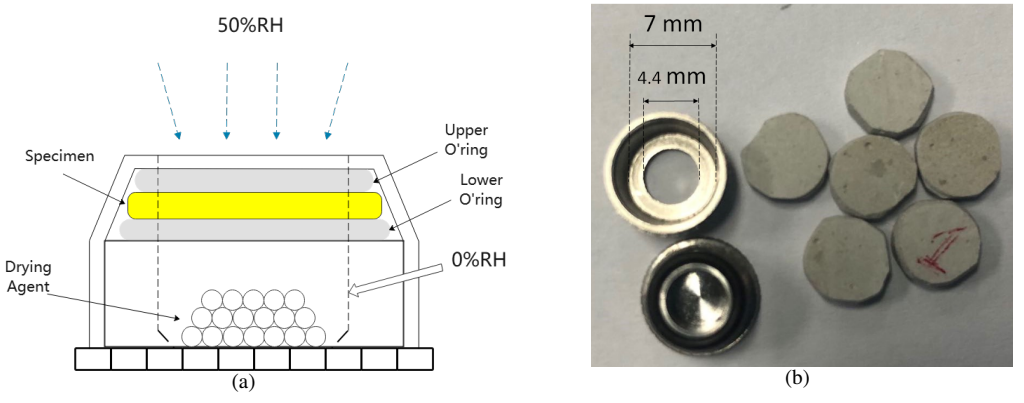

Figure 3: Vapor diffusivity measurement through DVS device: (a) arrangement of vapor diffusion test, and (b) cement paste specimens and diffusion (Payne) cell. The drying agent used is anhydrous calcium chloride ($CaCl_2$).

agent, anhydrous $CaCl_2$ in this study, to maintain nearly 0% RH. The pellet specimens were drilled out from the square slice specimens after freeze-drying, cf. Figure3b. The Payne cell, loaded with drying agent and pellet specimens, was put into the chamber of DVS device with temperature controlled to 25^{o}C and RH regulated to 50%. The total mass of Payne cell was weighed continuously, and the mass of vapor flowing into the cell was deduced from the gain of weight of Payne cell. From the measurement, the vapor diffusivity D_v was evaluated from the steady flow of water vapor across the exposed area of pellet specimens (15.54mm^2) under the constant RH gradient of 0-50%, expressed through the following equation[33],

$$D_v = \frac{RT}{M}\frac{e}{p_{vs}\Delta h}J_v \tag{1}$$

Here the term R stands for the ideal gas constant, T for the absolute temperature (25°C), M for the molar mass of water, J_v for the vapour mass flux through the diffusion surface, e for the thickness of specimen, p_{vs} for the saturated water vapour pressure at 25°C and Δh for the difference of RH (50%). The steady state of flow is judged from the mass evolution of Payne cell until the relative change of flow rate during two consecutive minutes is inferior to 1%, cf. Figure 4. The 0-50% RH gradient is chosen to trade off the experiment duration and the measurement precision. According to Kelvin's equation[34], the water vapour can condensate in pores of diameter smaller than 3nm at RH=50%, and the liquid water may also exist in pores as adsorbed water film on pore walls[35]. In other words, under the imposed RH gradient 0-50% most pores in cement paste, with size around 10-1000nm, are open for vapor diffusion.

A mercury porosimeter of Micromeritics' AutoPore (IV 9500 series) is used to determine the pore size distribution (PSD) of cement paste specimens. The instrument is capable of exerting an intrusion pressure in the range of 3.5 kPa-414 MPa corresponding to intruded pore diameters between 400μm-3.7nm in hardened cement pastes. For each MIP test, one freeze-dried square slice specimen was crushed into particles and collected into the intrusion chamber. The PSD curves were obtained from the intrusion volume of mercury and the contact angle between mercury and cement paste. Actually the MIP method measures the sizes of accessible path of the pore structure rather than its real geometry, but the measurement is still useful for comparison purpose[36, 37].

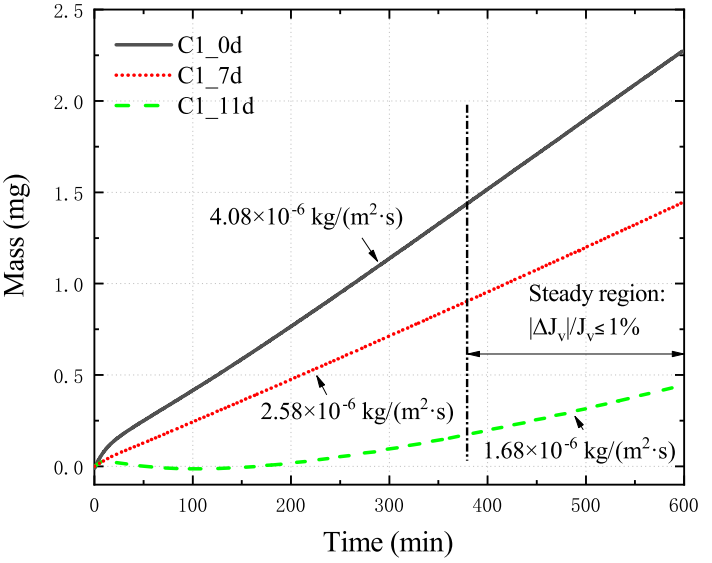

Figure 4: Mass evolution of Payne cell containing cement paste specimen (w/c=0.55) for 0d (black solid line), 7d(red dot line) and 11d (grain dash line) exposure to 10g/L SO_4^{2-}. The steady flow is reached as the slope becomes constant.

The expansion was measured on the rectangular slice specimens, 3 specimens for each solution, and the average of three specimens was taken as the expansion strain. The expansion was recorded continuously on weekly basis by a micrometer set with a precision of 1μm measuring the distance change between the two stuck pins. Due to the very thin thickness of the rectangular slices (2mm), the specimens yielded more or less out of plane curving in the later phase of ESA expansion as large amount of AFt is formed. To minimize this error, a total of 9 specimens were initially prepared for each solution and three specimens with the least curving effects were retained for the above expansion analysis.

3. Results

3.1. Aluminum phase contents

The relative contents of aluminum phases, expressed in percentage % of aluminum atoms in total aluminum phases, were derived from the two-range ^{27}Al NMR spectra in Figure 1 through the multi-phases fitting method in Figure 2. All the five aluminum phase contents in cement paste are presented in Figure 5 for three exposure solutions and different exposure ages. As aforementioned, the Al(IV) and Al(V) phases are incorporated in CSH structure at different sites, and their contents, about 5-10%, are relatively small compared to other aluminum phases[38]. Thus, the contents of these two phases are merged together in the results, denoted as Al(IV,V). For C1 solution in Figure 5a, the AFt content augments with time accompanied by a drop of AFm and Al(IV,V) contents while the TAH content fluctuates between 8-18% during the first 56d immersion and decreases to 4% at 84d. For C2 and C3 solutions in Figure 5b and 5c, the contents of AFt, AFm and Al(IV,V) evolve in the same pattern as C1 solution but with much less AFt detected at 84d. Globally, the results in Figure 5 confirm the transformation from AFm and Al(IV,V) phases to AFt phase, and this transformation is still in kinetic phase after 84d-168d immersion.

Figure 6 illustrates the impact of chlorides on the evolution of aluminum phases. First, the presence of chlorides reduces notably the AFt content at the same exposure ages, cf. Figure 6a. Second, the higher chloride concentration in C3 solution results in a larger inhibiting effect on the AFt formation. This is a direct experimental evidence for the inhibiting effect of chlorides on AFt formation. Third, the content of AFm phases shows no systematic difference for the three solutions in Figure 6b, and the TAH content is systematically higher in mixed solutions, cf. Figure 6c. Finally, the content of Al(IV,V) phases seems to be less consumed in the mixed solutions, cf. Figure 6d. A synthesis of these results reveals that a significant amount of AFm phase transforms to TAH phase, besides AFt phase, in mixed solutions. Thus, these results seem to support following mechanism: a significant amount of AFm phase and a small quantity of Al(IV,V) phase are converted to AFt phase when exposed to sulfate-containing solution, and the presence of chlorides converts part of AFm phase into TAH, resulting in less AFt formation.

The transformation from AFm phases to AFt under mixed solutions merits further discussion. Indeed, the AFm phases in hardened cement pastes refer to a family of aluminium(A)-ferrite(F) hydrates with a double-layered structure,

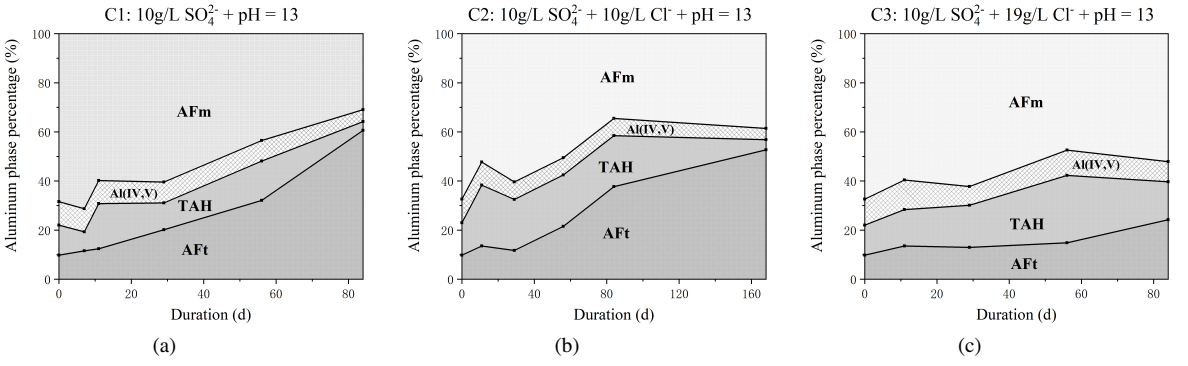

Figure 5: Aluminum phase contents in cement paste specimens exposed to C1 (a), C2(b) and C3 (c) solutions at different exposure ages. Al(IV,V) represents the sum of IV and V aluminum phases.

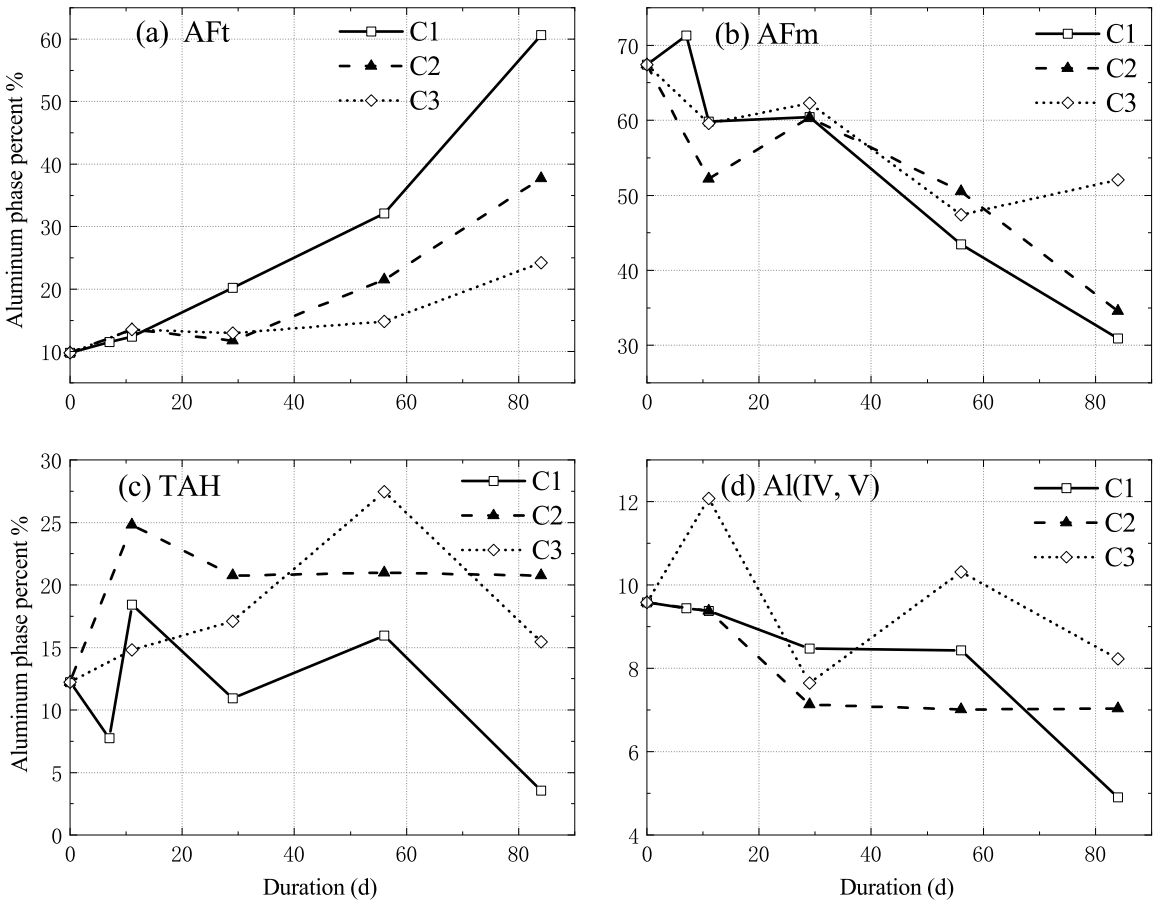

Figure 6: Contents of AFt (a), AFm (b), TAH (c) and Al(IV,V) (d) phases in cement paste specimens exposed to three solutions. C1 stands for 10g/L SO_4^{2-} solution, C2 for 10g/L SO_4^{2-} + 10g/L Cl^- solution, and C3 for 10g/L SO_4^{2-} + 19g/L Cl^- solution.

having a general formula $[Ca_2(Al,Fe)(OH)_6]\cdot X\cdot xH_2O$, where X denotes one formula unit of a single-charged anion or a half double-charged anion, and x is the interlayer water content conditioned by the temperature and RH at exposure[39]. Depending on the chemical environments, the double-layered structure could incorporate different anions to form different AFm species, such as monosulfoaluminate ($Ca_4[Al(OH)_6]_2\cdot SO_4 \cdot xH_2O$, denoted as Ms(6+$x$)), hydroxy-AFm ($Ca_4[Al(OH)_6]_2\cdot(OH)_2 \cdot xH_2O$, denoted as C_4AH_{7+x}) and Friedel's salts ($Ca_4[Al(OH)_6]_2\cdot Cl_2\cdot 4H_2O$, denoted as $C_4ACl_2H_{10}$)[40]. Due to the similar layered structure in these AFm species, i.e. almost same chemical environments for Al atom, the positions of their peaks in ^{27}Al NMR spectrum are very close ($\sim$ 1 ppm) compared to their peak widths ($\sim$10 ppm)[41]. Therefore, an extremely high spinning speed would be necessary to reduce their peak widths and separate these different AFm species. These different AFm species cannot be identified from the ^{27}Al NMR spectra in this study. Actually, the OH-SO_4-AFm solid solution, solution of Ms(6+x) and C_4AH_{7+x}, is the most common aluminum hydrates in ordinary cement pastes[42, 43]. When subject to mixed solution of sulfates and chlorides, the OH-SO_4-AFm tends to concurrently convert into AFt and $C_4ACl_2H_{10}$. Birnin-Yauri and Glasser[44] reported that only $\sim$14 mM chlorides are required to convert C_4AH_{7+x} to $C_4ACl_2H_{10}$ completely. Therefore, it is reasonable to assume

that the AFm species are OH-SO_4-AFm in C1 solution but $C_4ACl_2H_{10}$ and Ms(6+x) in C2/C3 solutions. On this basis, the transformation from AFm phases to AFt in three solutions involves the following reactions,

$$\begin{aligned} &C_4AH_{7+x} + 3CH + 3SO_4^{2-} \longrightarrow AFt + 6OH^- \\ &Ms(6+x) + 2CH + 2SO_4^{2-} \longrightarrow AFt + 4OH^- \\ &C_4ACl_2H_{10} + 2CH + 3SO_4^{2-} \longrightarrow AFt + 4OH^- + 2Cl^- \end{aligned} \tag{2}$$

The first two reactions occur in pure sulfate solution (C1) while the last two equations happen in mixed solutions (C2,C3). The supersaturation of AFt, β_{AFt}, can be taken as the driving force for crystallization process, defined through,

$$\beta_{AFt} = \frac{\left(a_{Ca^{2+}}\right)^6 \left(a_{OH^-}\right)^4 \left(a_{SO_4^{2-}}\right)^3 \left(a_{Al(OH)_4^-}\right)^2}{K_{AFt}} \tag{3}$$

with K_{AFt} standing for dissolution constant of AFt and a_i the ionic activity for species i. As the first approximation, the pore solution is regarded as a dilute solution and the ionic activity a_i is numerically equal to the ionic concentration c_i.

Now we attempt to quantify the supersaturation β_{AFt} for this study. The pore solution of specimens of 2mm thickness can be assumed to be in equilibrium with the solutions during the expansion. Thus, the concentrations of OH^- and SO_4^{2-}, c_{OH^-} and $c_{SO_4^{2-}}$, can take the values of solutions. The calcium and aluminate ions needed to form AFt are provided by CH and AFm phases respectively. Assuming the rapid dissolution of CH and AFm phases, these two phases are at their dissolution equilibria before they are depleted [45],

$$\begin{cases} \beta_{CH} = \dfrac{\left(c_{Ca^{2+}}\right)\left(c_{OH^-}\right)^2}{K_{CH}} = 1 \\ \beta_{C_4AH_{7+x}} = \dfrac{\left(c_{Ca^{2+}}\right)^4 \left(c_{OH}\right)^4 \left(c_{SO_4^{2-}}\right)\left(c_{S,Al(OH)_4^-}\right)^2}{K_{C_4AH_{7+x}}} = 1 \\ \beta_{C_4ACl_2H_{10}} = \dfrac{\left(c_{Ca^{2+}}\right)^4 \left(c_{OH}\right)^4 \left(c_{Cl^-}\right)^2 \left(c_{Cl,Al(OH)_4^-}\right)^2}{K_{C_4ACl_2H_{10}}} = 1 \end{cases} \tag{4}$$

where β_i and K_i denote the supersaturation and dissolution constant of phase i, and $c_{S,Al(OH)_4^-}$ and $c_{Cl,Al(OH)_4^-}$ stand for the aluminate concentration in pure sulfate solution and mixed solution respectively. Taking typical values of dissolution constants in literature [46], the aluminate concentration $c_{Al(OH)_4^-}$ in C1,2,3 is determined as 0.380 mmol/L, 0.019 mmol/L and 0.010 mmol/L for C1/2/3 solutions respectively. Substituting these values into Eq.3 gives the β_{AFt} values as 8.34×10^{11} (C1), 2.09×10^{9} (C2) and 5.79×10^{8} (C3). Such a decrease of driving force for crystallization, β_{AFt} in terms of the chloride concentration c_{Cl^-}, coincides with the decrease of the AFt formation rate with chloride concentration in Figure 6a.

3.2. Pore structure

Figure 7 presents the PSD evolution of specimens exposed to the three solutions. For the cement paste specimens before immersion (0d), three peaks are present: peak I with a typical diameter of 2-4nm, peak II with a typical diameter around 20-30nm and peak III around 80-100nm. For Portland cement (CEM I) pastes, the peak I and the peak II can be interpreted as the pores of inner and outer CSH respectively[47, 48], denoted as nanopores and micropores, and the pores around these two peaks constitute pores of CSH hydrates[49]. The peak III, much larger in size, corresponds to the capillary pores, resulting from the initial water-filled space not occupied by hydrates during hardening[39]. Usually, the capillary pore volume will decrease with hydration and the peak III will disappear[37, 50]. The appearance of peak III in Figure 7 is due to the high w/c ratio (0.55) of cement paste, resulting in a large portion of residual space among the hydrated cement grains[50]. For specimens immersed in three solutions, the peak II decays with time and even disappears after 84d, indicating an important structural change of micropores. Moreover, the peak III shifts towards

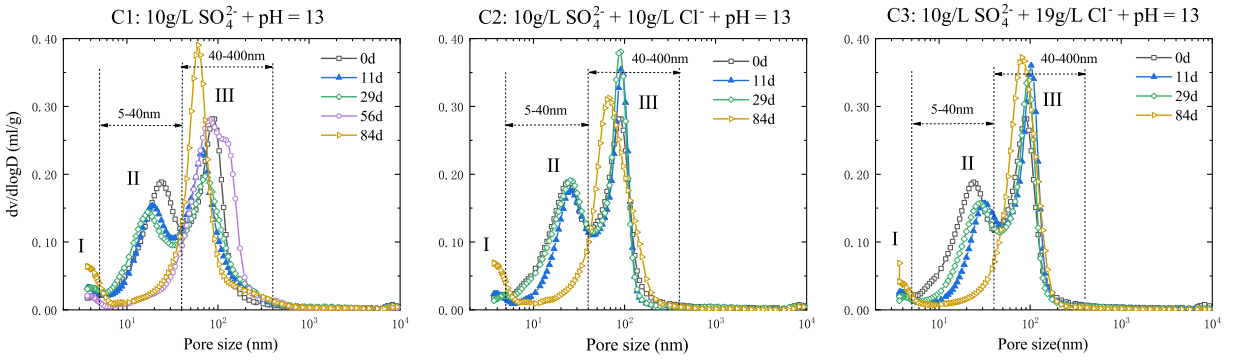

Figure 7: Pore size distribution of cement paste specimens exposed to C1 (a), C2 (b) and C3 (c) solutions at different exposure ages.

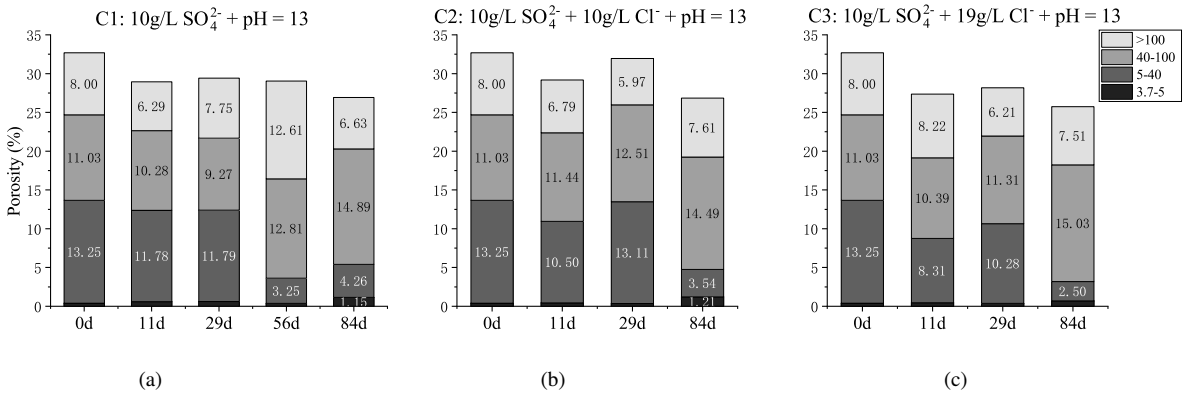

Figure 8: Pore volume of cement paste specimens exposed to C1 (a), C2 (b) and C3 (c) solutions at different exposure ages.

smaller sizes with immersion time reveals the crystallization of AFt also change the geometry of pores in this range.

Figure 8 shows directly the change of pore volume in four size ranges, derived from the PSD results in Figure 7. The pores of four size ranges are illustrated in Figure 9: the range 3.75-5nm refers to the pores in compact CSH (inner CSH) situated on the surface of unhydrated cement grains; the range 5-40nm refers to the pores in or enclosed by the less compacted CSH (outer CSH) situated next to inner CSH, connected to larger capillary pores and exposed to pore aqueous solution; the range 40-100nm refers to the capillary pores and probably microcracks; the range above 100nm refers to the large capillary pores, defects and microcacks[51]. Then, let us look into the change of pores in different size ranges with the help of the measured phase contents to shed new light on the pore crystallization of AFt. For nanopores (3.7-5nm), though small in quantity, increases systematically with time. This increase is related to the AFt formation[27] and the relevant change in the microstructure of CSH [28],

$$\mathrm{AFm} + \mathrm{Ca}^{2+} + \mathrm{SO}_4^{2-} \longrightarrow \mathrm{AFt} \tag{5}$$

In these nanopores, neither CH or AFt crystals are plausible to exist, and the AFm phases are assumed to grow preferably in outer CSH [39]. Thus, as AFt crystals form near the boundary of inner-outer CSH, cf. Figure 9b, the inner CSH can release Ca^{2+} ions to the reaction in Eq.5, leading to the decalcification of inner CSH. This mechanism may address the systematic increase of nanopores with sulfate exposure age. For the micropores (5-40nm), the pore

volume is substantially decreased for all cases with exposure ages. The pore space in this range can include both the intrinsic pores of outer CSH (Figure 9b) and the space enclosed by outer CSH forming an "ink-bottle" shape (Figure 9a). Since all reactants for AFt formation are present in outer CSH, the AFt crystals most likely form here, resulting in the substantial decrease of pores in this range due to the filling effect of AFt crystallization[52]. For capillary pores (40-100nm), the pore volume is globally increased with exposure age. Several factors can interplay during the AFt formation: the crystals of AFm phases and CH exist extensively[53], the AFt formation in Eq.5 consumes these crystals, and a trade-off between the pore filling by AFt crystallization and other crystals consumption accounts for the final pore volume change; moreover, if microcracking occurs during crystallization, e.g. from the crystallization in micropores, the formed microcracks can add to the pore volume in this range if 100nm is taken as the typical size for microcracks[54]. Quantitative analysis will be given in the following to clarify this point. For large capillary pores (>100nm), the pore volume is relatively stable, involving also the consumption of CH/AFm crystals, the AFt formation, the formation of microcracks, and the formation of gypsum in newly formed cracks as well[55]. Compared to C1 solution, the specimens in C2/C3 solutions present smaller volume for nanopores (3.75-5nm) and micropores (5-40nm), but comparable capillary pores and possibly microcracks (40-100nm, and >100nm) at 84d of exposure.

To investigate further the AFt crystallization in pores, a quantitative analysis is attempted for C1 solution using the phase content data in Figure 5a and pore volume data in Figure 8a. Since leaching and carbonation were screened out during immersion, the pore volume change is only related to the AFt crystallization and the dissolution of AFm phases and CH. As aforementioned, the AFm phases in C1 solution can be taken as OH-SO_4-AFm, a mixture of $C_4AH_{(7+x)}$ and Ms(6+x). To simplify the calculation, we assume the interlayer water content x to be 6 [39] and the minerals in cement to be completely hydrated. The relative ratio of C_4AH_{13} and Ms12 in OH-SO_4-AFm can be evaluated from the mole balance of Al and S elements,

$$\begin{cases} n_{SO_3} = 3n_{AFt} + n_{Ms12} \\ n_{Al_2O_3} = n_{AFt} + n_{Ms12} + n_{C_4AH_{13}} \\ n_{AFm} = n_{Ms12} + n_{C_4AH_{13}} \end{cases} \tag{6}$$

with n_i standing for the mole content i per unit volume of hardened cement paste. The values of n_{SO_3} and $n_{Al_2O_3}$ are determined from chemical composition of cement in Table 1, and n_{AFt} and n_{AFm} can be read from Figure 5a. The ratio of n_{Ms12} to $n_{C_4AH_{13}}$ is thus determined as 7:3. This ratio gives the equivalent molar volume of OH-SO_4-AFm as 0.30 L/mol by taking the literature values for the molar volumes of C_4AH_{13} (0.27 L/mol) and Ms12 ((0.31 L/mol))[46], and a consumption of 2.3 moles of CH per mole of OH-SO_4-AFm in AFt formation. From C1 immersion at 29d in Figure

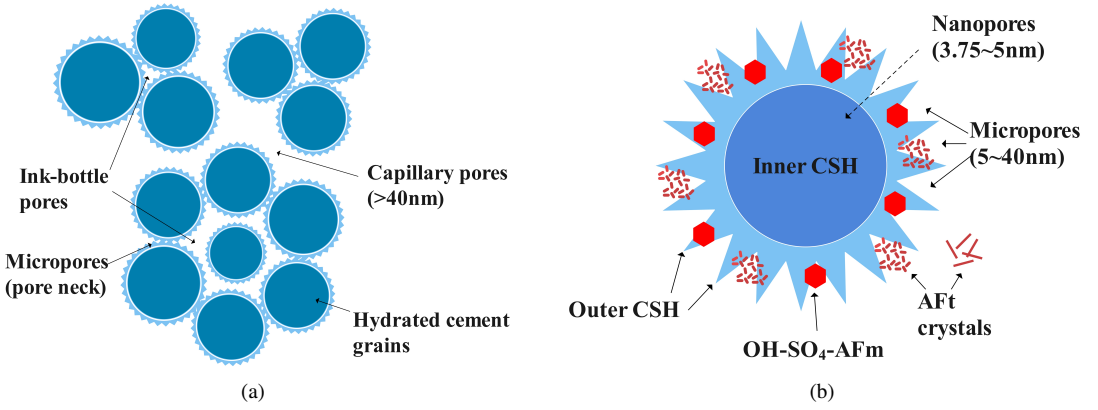

Figure 9: Illustration of pore structure of cement paste with high w/c ratio (0.55) (a) and cement grain after hydration (b). On the left, the capillary pores represent the connected space not occupied by hydrated solid phases, and the "ink-bottle" pores refer to the space enclosed by cement hydrates with the entry size belonging to the micropore range. On the right, the CSH hydrates are divided into inner and outer parts, the AFm phases exist most likely in outer CSH[39], and the AFt crystals precipitate both in micropores in the outer CSH and capillary pores.

5a, the newly formed AFt crystals amount to 0.057 mol/L, consuming 0.131 mol/L CH and dissolving 0.042 mol/L OH-SO_4-AFm. Thus, the AFt crystals fill out 4.05%, the dissolution of OH-SO_4-AFm and CH releases 1.69% and total pore volume change is -2.36% (decrease). The volume change of micropores (5-40nm), -1.46% in Figure 8a at 29d, indicates that AFt crystals do not precipitate only in micropores. The volume change of capillary pores (40-100nm), -1.76% in Figure 8a at 29d, confirms the AFt formation in these pores with dissolution of AFm/CH. Following the same line, the increase of 40-100nm volumes in C2/C3 solutions before 29d is due to fewer AFt formation and higher AFm consumption in Figure 6a and b. From Figure 5a for 29d to 56d, the AFt formation leads to -4.68% volume change and the dissolution of OH-SO_4-AFm/CH induces change of 3.32%. The volume of micropores (5-40nm) drops as much as -8.54% in Figure 8a from 29d to 56d, indicating that at least 3.86% micropore volume is not induced by AFt formation. The possible cause can be attributed to the pores of ”ink-bottle” shapes in Figure 9a: the ”ink-bottle” structure is enclosed by hydrated solids with the pore neck size entering the range of micropores. If the AFt formation, together with AFm/CH consumption, blocks this pore neck, no mercury can be intruded into the enclosed space and this pore volume may account for the large reduction of micropores. Such explanation can also support the significant decrease of micropore (5-40nm) volume 84d when immersed in C2/C3 solutions.

After the above analysis, the crystallization of AFt in pores can be summarized as follows: AFt crystals precipitates in both micropores and capillary pores, AFm phases and CH dissolve more in capillary pores. With exposure age, the AFt crystals block the pore necks of "ink-bottle" pores, resulting in a significant reduction in pore volume in micropore (5-40nm) range. The accumulation of AFt crystals in pores, especially in the micropore range, fractures the solid matrix of hardened cement paste and reopen the "ink-bottle" pores in Figure 9a, and these microcracks and the reopened "ink-bottle" pores most likely join the pore ranges of 40-100nm or >100nm. The presence of chlorides delays this process by reducing both the rate and the quantity of AFt formation. Thus, the dissolution of AFm phases and CH in C2/C3 solutions contributes more to the pore space release in the range of 40-100nm compared to C1 solution.

3.3. Vapour diffusivity

The vapour diffusivity D_v is presented in Figure 10 for pellet cement paste specimens immersed in C1 and C2 solutions at different exposure ages. The water vapour diffusivity was reported as being in the range of 0.1-1×10^{-7} m^2/s under a RH gradient of 0-50% over a thickness of 30mm for concrete specimens[56]. Baroghel-Bouny[57] measured

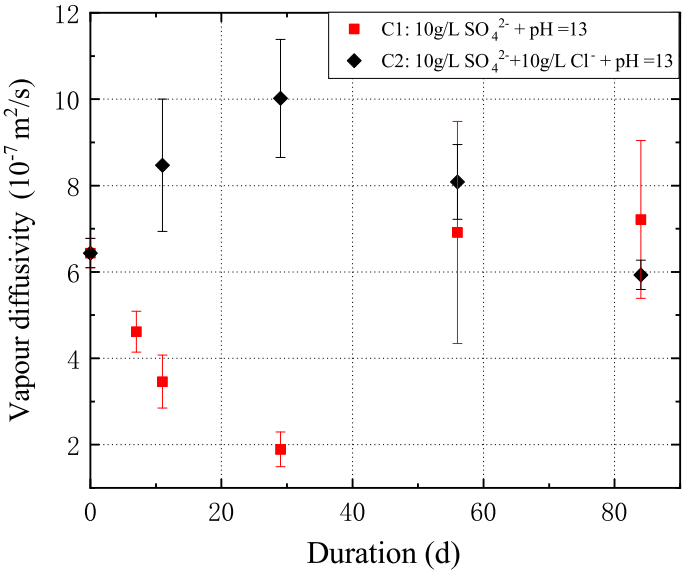

Figure 10: Vapour diffusivity of cement paste specimens exposed to C1 and C2 solutions at different ages.

the apparent vapour diffusivity D_v in the range of 1-10×10^{-7} m^2/s for the pore saturation range 0.1-0.5, the same order of magnitude as D_v in Figure 10.

In C1 immersion, the D_v values decrease until 28d and then rise up to 84d, corresponding to the reduction of pores in the ranges of 5-100nm before 28d and the increase of pores larger than 100nm after 56d in Figure 8a, respectively. The reduction of D_v in the early phase of ESA is caused by the refinement of pore structure, due to the synergic effect of AFt formation and AFm/CH dissolution, in pores of 5-100nm. The subsequent rise of D_v after 28d, along with more AFt formation, indicates the appearance of microcracks in solid matrix of cement paste, which provides a more direct and quick diffusion path for vapor transport. In C2 immersion from 0d to 29d, the pore volume of 5-100nm in Figure 8b underwent a more complex change: a slight volume decrease (-0.14%) in 5-40nm pores and relatively large volume increase (1.48%) in 40-100nm pores with important dissolution of AFm phases and CH. The larger diffusivity at 29d compared to 0d is due to this pore space release. The subsequent decrease of vapor diffusivity, from 29d to 84d exposure, is closely related to the important pore volume change in the 5-40nm range, -9.57% from Figure 8b. As aforementioned, this pore volume reduction reflects the blockage of pore necks for “ink-bottle” pores, cf. Figure 9a. Afterwards, the enclosed "ink-bottle" pores is inaccessible either to MIP or to vapour transport. In summary, the AFt formation and the related AFm/CH consumption in pores are to reduce the transport rate of pore matters before the appearance of microcracks. Actually, this reduction has been observed in literature for other transport properties [58]. Once the microcracking occurs, this reduction can be totally cancelled out by the new transport channels for pore matters. Comparing C1 and C2 immersion cases, one can see that the presence of chlorides offsets this reduction effect, before microcracking, even increases the vapor diffusivity by dominating AFm/CH consumption.

3.4. Expansion

Figure 11 shows the expansion behaviour of cement paste specimens exposed to the three solutions C1-C3. Under sulfate immersion, the specimens all show progressive expansion but with different patterns for C1 and C2/C3 solutions. The expansion in C1 solution occur in two stages: a first expansion growth stage with moderate and linear expansion rate till 56d, named also as "induction phase"[59], and second stage with much faster expansion rate. By contrast, the expansion of C2/C3 specimens undergoes only the linear growth phase of expansion. During the expansion measurement, the C1 specimens fractured after the second stage until a rather large strain for expansion ∼1.1% was

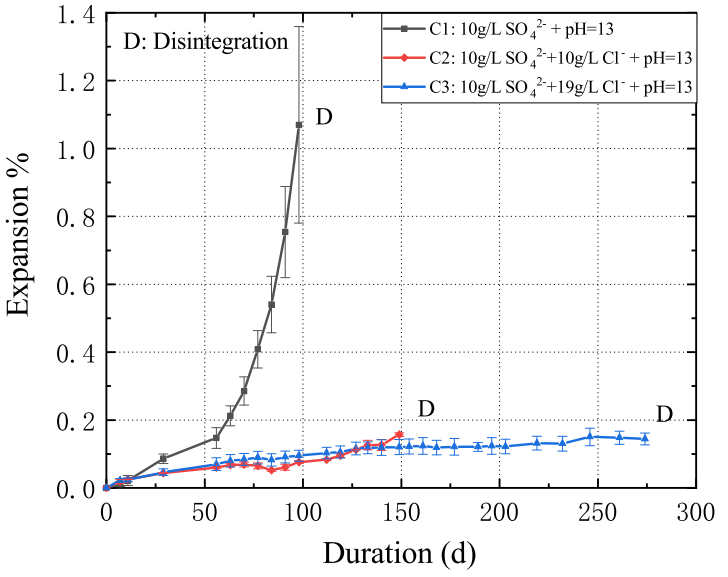

Figure 11: Expansion of cement paste specimens exposed to three sulfate solutions.

reached while the specimens in C2/C3 were broken right after the linear stage at much smaller strain ~0.15%, indicating that the microcracks are far more developed in C1 specimens than C2/C3 specimens. Note that the tensile strain at the end of first stage for all specimens, in the order of 0.15%, is one order of magnitude larger than the maximum tensile strain that the hardened cement pastes can sustain during a uniaxial tensile test[60]. This means, through the first stage of expansion scales linearly with exposure time, the specimens have largely passed the pure elastic region of stress-strain relationship of the solid matrix and contain microcracks from AFt formation. The relevance of AFt quantity to the expansion magnitude is to be discussed later. As we compare the expansions of C1 specimens with C2/C3 specimens, the inhibiting effect of chlorides on ESA expansion is obvious, which is in line with the available literature results [2, 10, 12]. Moreover, this inhibiting effect becomes more important with the chloride concentration. The influence of chlorides on expansion coincides with the effect of chlorides on AFt formation rate in Figure 6a, indicating that the crystallization of AFt is the mechanical reason for expansion.

4. Further discussion

4.1. Sulfate attack in pure sulfate solution and crystallization pressure of AFt crystals

Figure 12 synthesizes the evolution of AFt content, vapour diffusivity and expansion of cement paste specimens exposed in C1 solution. The exposure age of 56d constitutes a critical point for all results: before this age the AFt has clear filling effect in porosity decreasing substantially the vapor diffusivity, and afterwards, cf. Figure 12, the rate of AFt formation increase leads to much faster expansion and a jumping change of order of magnitude for vapour diffusivity, accompanied by notable increase of pores in the range >100 nm in Figure 8a. On this basis, a two-stage chemo-mechanical mechanism for sulfate attack can be formulated for the specimens as follows.

In the first stage within 56d exposure, the external sulfates react with aluminum phases in cement pastes to produce expansive product (AFt crystals), in pores in the range of 5-100 nm. These crystals fill the pore volume and thus reduce the vapor transport property on the one hand, and generate internal pore pressure leading to a slow expansion rate on the other hand. With the formation of AFt crystals going on, the internal pore pressure builds up high enough, more likely in the pore necks within the micropore range (5-40nm), to fracture the solid matrix of cement paste inducing microcracks and reopen the enclosed “ink-bottle" pores. The appearance of microcracks changes cement paste from

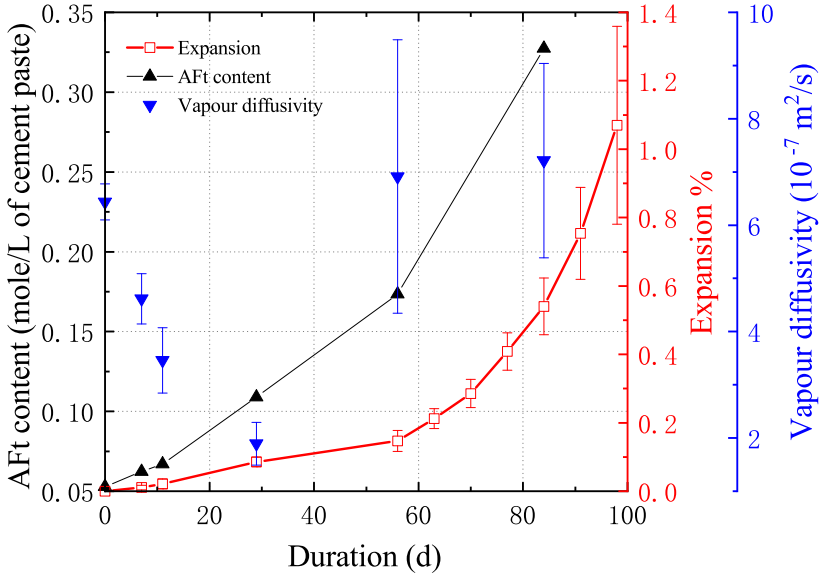

Figure 12: AFt content (black), expansion (red), and vapour diffusivity of cement paste specimens exposed to C1 solution.

porous continuum to discrete one. These microcracks and the reopened “ink-bottle" pores add to the pore volume increase around sizes of 100nm, and also soften the solid matrix providing an elastic modulus lower and lower. The former results in a large vapour diffusivity and the latter corresponds to a faster expansion.

The mechanical reason for expansion is the pressure arising from the AFt crystallization in pores (confined space). This crystallization pressure is needed to keep the mechanical equilibrium of crystals during the growth in pores and overcome the the interface energy barrier between the crystal and pore liquid[61]. Given a *cylindrical* pore, the pressure on AFt crystals P_C is related to the radius of pore entry size r by the Laplace equation:

$$P_C - P_L = \frac{2\gamma_{CL}}{r} \tag{7}$$

where P_L stands for pressure of liquid phase and γ_{CL} for the surface energy of crystal-liquid interface, taking 0.1 J/m^2[61]. Using this equation and assuming the liquid pressure P_L equal to the atmospheric pressure, the AFt crystal needs to be loaded with a pressure of 13.3-20.0 MPa to grow in pores of 20-30nm. This pressure is in turn, in equal values, exerted on the solid matrix of cement paste, constituting the mechanical origin for material expansion. Considering the magnitude of pressure and the pore geometry for crystal growth in Figure 9, the AFt crystallization in micropores can be assumed to be the major source of expansion.

4.2. AFt amount and expansion during linear stage

Both the crystallization pressure theory[45, 62] and the volume increase theory[63, 64] relate the expansion stress to the content of newly formed AFt crystals. In the present study, if the newly formed TAH in C2/C3 solutions in Figure 6c is assumed to be an amorphous phase[31], the AFt formation will be the only source to generate pore pressure. Figure 13 illustrates the specimen expansion strain in terms of the measured AFt content in three solutions during the linear expansion stage. In this stage, the expansion scales almost linearly with the AFt content but different slopes are observed for C1 solution and C2/C3 solutions. This difference in slopes, i.e. same quantity of AFt formation giving different expansion values, can be better interpreted through pore crystallization concepts. Actually, the crystallization pressure can be incorporated into the classical poromechanics[65], and the stress-free expansion by internal pore pressure accumulation can be expressed as,

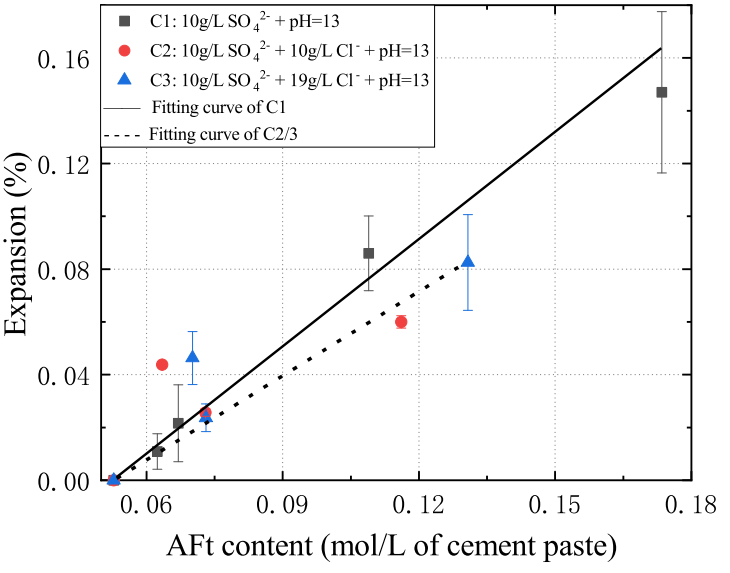

Figure 13: Expansion of cement paste specimens in terms of AFt content.

$$\sigma = 0 : 3K\epsilon_{\mathrm{ESA}} = bS_{\mathrm{C}}P_{\mathrm{C}} \quad \text{with} \quad S_{\mathrm{C}} = \frac{V_{\mathrm{C}}}{\phi_0} n_{\mathrm{AFt}} \tag{8}$$

with b standing for the Biot's coefficient, V_{C} for the molar volume of AFt crystals, S_{C} for the volume fraction of pore space occupied by AFt crystals, P_{C} for crystallization pressure, ϕ_0 for initial porosity of material, n_{AFt} for AFt content, K for bulk modulus and ϵ_{ESA} for free linear expansion strain under ESA. In this expression, we assume implicitly that the liquid phase pressure $P_{\mathrm{L}} = 0$, i.e. the liquid pressure serves as the reference for the solid phase. Therefore, the slopes in Figure 13 represent the ratio of ϵ_{ESA} to n_{AFt} and can be expressed as $[bV_{\mathrm{C}}/(3\phi_0 K)]P_{\mathrm{C}}$. The crystallization P_{C} can be evaluated following Corren's equation [66],

$$P_{\mathrm{C}} = \frac{RT}{V_{\mathrm{C}}} \ln\left(\beta_{\mathrm{AFt}}\right) \tag{9}$$

Substituting the estimated β_{AFt} in Section 3.1 into Eq. (9) gives P_{C} in C1, 2, 3 solutions as 95.83, 74.92, 70.44 MPa. By taking the typical values of mechanical properties (b, K) for hardened cement pastes in [67], the slops are determined as 9.93×10^{-6} (C1), 7.76×10^{-6} (C2) and 7.30×10^{-6} (C3). Compared to the measured slopes, 13.54×10^{-6} (C1), 10.90×10^{-6} (C2/C3), these estimates are very close and observe the same order of magnitude, which attributes the different slopes to the different crystallization pressures.

The above analysis can help to deepen the mechanism of mitigating effect of chlorides on ESA as such: adding chlorides in pore solution alters the dissolution equilibria in the multi-species aqueous environment[68], reducing the aluminate concentration $c_{\mathrm{Al(OH)_4^-}}$ and the supersaturation of AFt crystals β_{AFt}; these changes lead to the reduction both in AFt formation rate in Figure 6a and in the crystallization pressure P_{C}; the synthetic effect of AFt amount n_{AFt} decrease and P_{C} decrease results in a drop in expansion according to Eq.(8).

5. Conclusion

1, Quantitative ^{27}Al NMR examination confirms the mitigating effect of chlorides on AFt formation: the presence of chlorides converts part of AFm phases into TAH phase, reducing AFt formation, and a higher concentration of chlorides results in a slower AFt generation rate. The analysis on multi-phase dissolution equilibria in pore solution shows the reducing effect of chlorides on the supersaturation of AFt crystals, providing a possible explanation of the mitigating effect. Also through this depressing effect on the AFt supersaturation, the same quantity of AFt crystal formation does not generate the same level of crystallization pressure, giving lower expansion capacity of AFt crystals in mixed (C2/C3) solutions than in pure sulfate (C1) solution.

2. A synthetic analysis of phase content and pore structure confirms that AFt crystallization occurs in whole range of pore space of hardened cement paste. The comparison of pore volume filling by AFt formation, from ^{27}Al NMR data, and pore space reduction, detected by MIP in 5-40nm size range, reveals the role of "ink-bottle" pores in the pore volume change. The AFt crystals, formed in the micropores of interposed outer CSH from different cement grains, fill up the neck pores and block the enclosed pore space, resulting in a substantial decrease in 5-40nm pores. In the range of 40-100nm, the AFt precipitation and AFm/CH dissolution interplay together to influence the pore volume. The microcracks created by AFt formation and the reopened "ink-bottle" pores eventually join the measured pore volume around the size 100nm.

3. The pore crystallization of AFt leads to the corresponding change in transport property and mechanical behavior. In the pure sulfate (C1) solution, the pore-filling by AFt crystals causes a decrease in vapour diffusivity, and the subsequent AFt formation induces microcracks and augments the vapour diffusivity. The presence of chlorides offsets the pore-filling of AFt formation in early exposure even increases the vapour diffusivity due to the synthetic effect from AFm/CH dissolution. The AFt crystallization in the pore-neck part of micropores would be the direct source for pore pressure generation and material expansion. The specimen expansion is closely related to the evolution of measured AFt content. The linear expansion stage is well captured by the classical promechanics and the lower expansion with chlorides is addressed by the depressed AFt supersaturation.

Acknowledgement

The research is supported by China National Science Foundation Grant No. 52038004. The first author benefits from a mutual doctoral program between Tsinghua university (China) and Université Gustave Eiffel (France). The assistance of Dr. Haiyun Yang, in Analysis Center of Tsinghua University, is acknowledged for his guidance in the NMR measurement of cement paste specimens.

References

[1] M. Santhanam, M. Cohen, J. Olek, Differentiating seawater and groundwater sulfate attack in portland cement mortars, Cement and Concrete Research 36 (2006) 2132–2137. doi:https://doi.org/10.1016/j.cemconres.2006.09.011.

[2] J. O. Ukpata, P. Muhammed Basheer, L. Black, Expansion of cem i and slag-blended cement mortars exposed to combined chloride-sulphate environments, Cement and Concrete Research 123 (2019) 105794. doi:https://doi.org/10.1016/j.cemconres.2019.105794.

[3] O. S. B. Al-Amoudi, Sulfate attack and reinforcement corrosion in plain and blended cements exposed to sulfate environments, Building and Environment 33 (1998) 53–61. doi:https://doi.org/10.1016/S0360-1323(97)00022-X.

[4] J. Skalny, P. Brown, Sulfate attack on concrete, Taylor & Francis, 2002.

[5] U. Angst, B. Elsener, C. K. Larsen, Øystein Vennesland, Critical chloride content in reinforced concrete — a review, Cement and Concrete Research 39 (2009) 1122–1138. doi:https://doi.org/10.1016/j.cemconres.2009.08.006.

[6] Z. Jin, W. Sun, Y. Zhang, J. Jiang, J. Lai, Interaction between sulfate and chloride solution attack of concretes with and without fly ash, Cement and Concrete Research 37 (2007) 1223–1232. doi:https://doi.org/10.1016/j.cemconres.2007.02.016.

[7] M. Maes, N. De Belie, Resistance of concrete and mortar against combined attack of chloride and sodium sulphate, Cement and Concrete Composites 53 (2014) 59–72. doi:https://doi.org/10.1016/j.cemconcomp.2014.06.013.

[8] K. De Weerdt, D. Orsáková, M. Geiker, The impact of sulphate and magnesium on chloride binding in portland cement paste, Cement and Concrete Research 65 (2014) 30–40. doi:https://doi.org/10.1016/j.cemconres.2014.07.007.

[9] J. Geng, D. Easterbrook, L. yuan Li, L. wei Mo, The stability of bound chlorides in cement paste with sulfate attack, Cement and Concrete Research 68 (2015) 211–222. doi:https://doi.org/10.1016/j.cemconres.2014.11.010.

[10] O. S. B. Al-Amoudi, M. Maslehuddin, Y. A. Abdul-Al, Role of chloride ions on expansion and strength reduction in plain and blended cements in sulfate environments, Construction and Building Materials 9 (1995) 25–33. doi:https://doi.org/10.1016/0950-0618(95)92857-D.

[11] M. Zhang, J. Chen, Y. Lv, D. Wang, J. Ye, Study on the expansion of concrete under attack of sulfate and sulfate–chloride ions, Construction and Building Materials 39 (2013) 26–32. doi:https://doi.org/10.1016/j.conbuildmat.2012.05.003, special Issue: ISCCM 2011, Ningbo, China, November 7-9, 2011.

[12] S.-T. Lee, D.-W. Park, K.-Y. Ann, Mitigating effect of chloride ions on sulfate attack of cement mortars with or without silica fume, Canadian Journal of Civil Engineering 35 (2008) 1210–1220.

[13] K. M. A. Hossain, Performance of volcanic ash and pumice-based blended cements in sulphate and sulphate–chloride environments, Advances in Cement Research 18 (2006) 71–82. doi:10.1680/adcr.2006.18.2.71.

[14] W. M. Madgin, D. A. Swales, Solubilities in the system caso4-nacl-h2o at 25° and 35°, Journal of Chemical Technology & Biotechnology 6 (2007) 482–487.

[15] H. Corner, D. Rippstain, Effect of aqueous sodium chloride solution on ettringite, Touindustrie-Zeitung (TIZ) Fachberichte 9 (1985) 680–683.

[16] J. Johnston, C. Grove, The solubility of calcium hydroxide in aqueous salt solutions, Journal of the American Chemical Society 53 (1931) 3976–3991. doi:10.1021/ja01362a009.

[17] R. Robinson, R. Stokes, Electrolyte solutions, London, Butterworth, 1968.

[18] H. C. Helgeson, D. H. Kirkham, G. C. Flowers, Theoretical prediction of the thermodynamic behavior of aqueous electrolytes by high pressures and temperatures; iv, calculation of activity coefficients, osmotic coefficients, and apparent molal and standard and relative partial molal properties to 600°c and 5kb, American Journal of Science 281 (1981) 1249–1516. doi:10.2475/ajs.281.10.1249.

[19] D. A. Kulik, T. Wagner, S. V. Dmytrieva, G. Kosakowski, K. V. Hingerl, Ferdinand F. Chudnenko, U. R. Berner, Gem-selektor geochemical modeling package: revised algorithm and gems3k numerical kernel for coupled simulation codes, Computational Geosciences 17 (2013) 1–24. doi:10.1007/s10596-012-9310-6.

[20] I. Biczok, Concrete Corrosion and Concrete Protection, Chemical Publishing Company, 1967.

[21] J. Stroh, B. Meng, F. Emmerling, Deterioration of hardened cement paste under combined sulphate-chloride attack investigated by synchrotron xrd, Solid State Sciences 56 (2016) 29–44. doi:https://doi.org/10.1016/j.solidstatesciences.2016.04.002.

[22] M. Balonis, B. Lothenbach, G. Le Saout, F. P. Glasser, Impact of chloride on the mineralogy of hydrated portland cement systems, Cement and Concrete Research 40 (2010) 1009–1022. doi:https://doi.org/10.1016/j.cemconres.2010.03.002.

[23] G. Li, A. Zhang, Z. Song, S. Liu, J. Zhang, Ground granulated blast furnace slag effect on the durability of ternary cementitious system exposed to combined attack of chloride and sulfate, Construction and Building Materials 158 (2018) 640–648. doi:https://doi.org/10.1016/j.conbuildmat.2017.10.062.

[24] P. W. Brown, An evaluation of the sulfate resistance of cements in a controlled environment, Cement and Concrete Research 11 (1981) 719–727.

[25] C. Xiong, L. Jiang, Y. Xu, H. Chu, M. Jin, Y. Zhang, Deterioration of pastes exposed to leaching, external sulfate attack and the dual actions, Construction and Building Materials 116 (2016) 52–62. doi:https://doi.org/10.1016/j.conbuildmat.2016.04.133.

[26] R. H. Bogue, Calculation of the compounds in portland cement, Industrial & Engineering Chemistry Analytical Edition 1 (1929) 192–197.

[27] Y. Gu, R.-P. Martin, O. Omikrine Metalssi, T. Fen-Chong, P. Dangla, Pore size analyses of cement paste exposed to external sulfate attack and delayed ettringite formation, Cement and Concrete Research 123 (2019) 105766. doi:https://doi.org/10.1016/j.cemconres.2019.05.011.

[28] R. Ragoug, O. O. Metalssi, F. Barberon, J.-M. Torrenti, N. Roussel, L. Divet, J.-B. d'Espinose de Lacaillerie, Durability of cement pastes exposed to external sulfate attack and leaching: Physical and chemical aspects, Cement and Concrete Research 116 (2019) 134–145. doi:https://doi.org/10.1016/j.cemconres.2018.11.006.

[29] J.-B. d'Espinose de Lacaillerie, C. Fretigny, D. Massiot, Mas nmr spectra of quadrupolar nuclei in disordered solids: The czjzek model, Journal of Magnetic Resonance 192 (2008) 244–251. doi:https://doi.org/10.1016/j.jmr.2008.03.001.

[30] J. Skibsted, E. Henderson, H. J. Jakobsen, Characterization of calcium aluminate phases in cements by aluminum-27 mas nmr spectroscopy, Inorganic chemistry 32 (1993) 1013–1027.

[31] M. D. Andersen, H. J. Jakobsen, J. Skibsted, A new aluminium-hydrate species in hydrated portland cements characterized by 27al and 29si mas nmr spectroscopy, Cement and Concrete Research 36 (2006) 3–17.

[32] H. Garbalińska, M. Bochenek, W. Malorny, J. von Werder, Comparative analysis of the dynamic vapor sorption (dvs) technique and the traditional method for sorption isotherms determination — exemplified at autoclaved aerated concrete samples of four density classes, Cement and Concrete Research 91 (2017) 97–105. doi:https://doi.org/10.1016/j.cemconres.2016.11.001.

[33] V. Baroghel-Bouny, Water vapour sorption experiments on hardened cementitious materials. part ii: Essential tool for assessment of transport properties and for durability prediction, Cement and Concrete Research 37 (2007) 438–454. doi:https://doi.org/10.1016/j.cemconres.2006.11.017, cementitious Materials as model porous media: Nanostructure and Transport processes.

[34] W. Thomson, On the equilibrium of vapour at a curved surface of liquid, Proceedings of the Royal Society of Edinburgh 7 (1872) 63–68.

[35] K. Li, Durability design of concrete structures: Phenomena, modeling, and practice, John Wiley & Sons, 2016.

[36] H. Giesche, Mercury porosimetry: a general (practical) overview, Particle & particle systems characterization 23 (2006) 9–19.

[37] Q. Zeng, K. Li, T. Fen-chong, P. Dangla, Pore structure characterization of cement pastes blended with high-volume fly-ash, Cement and Concrete Research 42 (2012) 194–204. doi:https://doi.org/10.1016/j.cemconres.2011.09.012.

[38] R. Ragoug, Attaque sulfatique externe des matériaux cimentaires : Impact de différents facteurs âge, composition du liant, présence de chlorures, Theses, Université Paris-Est, 2016. URL: https://tel.archives-ouvertes.fr/tel-01552785.

[39] H. F. Taylor, et al., Cement chemistry, volume 2, Thomas Telford London, 1997.

[40] L. G. Baquerizo, T. Matschei, K. L. Scrivener, M. Saeidpour, L. Wadsö, Hydration states of afm cement phases, Cement and Concrete Research 73 (2015) 143–157. doi:https://doi.org/10.1016/j.cemconres.2015.02.011.

[41] K. Scrivener, R. Snellings, B. Lothenbach, et al., A practical guide to microstructural analysis of cementitious materials, volume 540, Crc Press Boca Raton, FL, USA:, 2016.

[42] T. Matschei, B. Lothenbach, F. Glasser, The afm phase in portland cement, Cement and concrete research 37 (2007) 118–130.

[43] F. Glasser, A. Kindness, S. Stronach, Stability and solubility relationships in afm phases: Part i. chloride, sulfate and hydroxide, Cement and Concrete Research 29 (1999) 861–866.

[44] U. Birnin-Yauri, F. Glasser, Friedel's salt, ca2al(oh)6(cl,oh)·2h2o: its solid solutions and their role in chloride binding, Cement and Concrete Research 28 (1998) 1713–1723. doi:https://doi.org/10.1016/S0008-8846(98)00162-8.

[45] Y. Gu, P. Dangla, R.-P. Martin, O. Omikrine Metalssi, T. Fen-Chong, Modeling the sulfate attack induced expansion of cementitious materials based on interface-controlled crystal growth mechanisms, Cement and Concrete Research 152 (2022) 106676. doi:https://doi.org/10.1016/j.cemconres.2021.106676.

[46] B. Lothenbach, D. A. Kulik, T. Matschei, M. Balonis, L. Baquerizo, B. Dilnesa, G. D. Miron, R. J. Myers, Cemdata18: A chemical thermodynamic database for hydrated portland cements and alkali-activated materials, Cement and Concrete Research 115 (2019) 472–506. doi:https://doi.org/10.1016/j.cemconres.2018.04.018.

[47] R. Vočka, C. Gallé, M. Dubois, P. Lovera, Mercury intrusion porosimetry and hierarchical structure of cement pastes: Theory and experiment, Cement and Concrete Research 30 (2000) 521–527. doi:https://doi.org/10.1016/S0008-8846(99)00252-5.

[48] C. Gallé, Effect of drying on cement-based materials pore structure as identified by mercury intrusion porosimetry: A comparative study between oven-, vacuum-, and freeze-drying, Cement and Concrete Research 31 (2001) 1467–1477. doi:https://doi.org/10.1016/S0008-8846(01)00594-4.

[49] V. Baroghel-Bouny, Caractérisation des pâtes de ciment et des bétons: méthodes, analyses, interprétations, Laboratoire Central des Ponts et Chausees, 1994.

[50] R. A. Cook, K. C. Hover, Mercury porosimetry of hardened cement pastes, Cement and Concrete Research 29 (1999) 933–943. doi:https://doi.org/10.1016/S0008-8846(99)00083-6.

[51] P. K. Mehta, P. J. Monteiro, Concrete: microstructure, properties, and materials, McGraw-Hill Education, 2014.

[52] W. Müllauer, R. E. Beddoe, D. Heinz, Sulfate attack expansion mechanisms, Cement and Concrete Research 52 (2013) 208–215. doi:https://doi.org/10.1016/j.cemconres.2013.07.005.

[53] A. C. A. Muller, Characterization of porosity & CSH in cement pastes by ^{1}H NMR, Technical Report, EPFL, 2014.

[54] S. Diamond, Microstructure of cement-based systems/bonding and interfaces in cementitious materials, in: Mat. Res. Soc. Symp. Proc., MRS, Pittsburgh, volume 370, 1995, p. 217.

[55] C. Yu, W. Sun, K. Scrivener, Mechanism of expansion of mortars immersed in sodium sulfate solutions, Cement and Concrete Research 43 (2013) 105–111. doi:https://doi.org/10.1016/j.cemconres.2012.10.001.

[56] M. Jooss, H. W. Reinhardt, Permeability and diffusivity of concrete as function of temperature, Cement and Concrete Research 32 (2002) 1497–1504. doi:https://doi.org/10.1016/S0008-8846(02)00812-8.

[57] V. Baroghel-Bouny, Water vapour sorption experiments on hardened cementitious materials. part ii: Essential tool for assessment of transport properties and for durability prediction, Cement and Concrete Research 37 (2007) 438–454. doi:https://doi.org/10.1016/j.cemconres.2006.11.017, cementitious Materials as model porous media: Nanostructure and Transport processes.

[58] P. J. Tumidajski, G. Chan, K. E. Philipose, An effective diffusivity for sulfate transport into concrete, Cement and Concrete Research 25 (1995) 1159–1163. doi:https://doi.org/10.1016/0008-8846(95)00108-0.

[59] M. Santhanam, M. D. Cohen, J. Olek, Effects of gypsum formation on the performance of cement mortars during external sulfate attack, Cement and Concrete Research 33 (2003) 325–332. doi:https://doi.org/10.1016/S0008-8846(02)00955-9.

[60] H. Zhang, B. Šavija, M. Luković, E. Schlangen, Experimentally informed micromechanical modelling of cement paste: An approach coupling x-ray computed tomography and statistical nanoindentation, Composites Part B: Engineering 157 (2019) 109–122. doi:https://doi.org/10.1016/j.compositesb.2018.08.102.

[61] G. W. Scherer, Stress from crystallization of salt, Cement and Concrete Research 34 (2004) 1613–1624. doi:https://doi.org/10.1016/j.cemconres.2003.12.034, h. F. W. Taylor Commemorative Issue.

[62] B. Bary, N. Leterrier, E. Deville, P. Le Bescop, Coupled chemo-transport-mechanical modelling and numerical simulation of external sulfate attack in mortar, Cement and Concrete Composites 49 (2014) 70–83. doi:https://doi.org/10.1016/j.cemconcomp.2013.12.010.

[63] R. Tixier, B. Mobasher, Modeling of damage in cement-based materials subjected to external sulfate attack. i: Formulation, Journal of Materials in Civil Engineering 15 (2003) 305–313.

[64] T. Ikumi, S. H. Cavalaro, I. Segura, A. Aguado, Alternative methodology to consider damage and expansions in external sulfate attack modeling, Cement and Concrete Research 63 (2014) 105–116. doi:https://doi.org/10.1016/j.cemconres.2014.05.011.

[65] O. Coussy, Mechanics and physics of porous solids, John Wiley & Sons, 2011.

[66] C. W. Correns, Growth and dissolution of crystals under linear pressure, Discussions of the Faraday society 5 (1949) 267–271.

[67] F. Ulm, G. Constantinides, F. Heukamp, Is concrete a poromechanics material, A multiscale investigation of poroelastic properties, Materials 420 (2004) 43–58. doi:https://doi.org/10.1007/BF02481626.

[68] M. Xie, P. Dangla, K. Li, Reactive transport modelling of concurrent chloride ingress and carbonation in concrete, Materials and Structures 54 (2021) 1–19. doi:https://doi.org/10.1617/s11527-021-01769-9.